Sensors & Actuators: B. Chemical 415 (2024) 135982

Contents lists available at ScienceDirect

Sensors and Actuators: B. Chemical

journal homepage: www.elsevier.com/locate/snb

Carbon functionalized cladding bismuth tungstate-based 3D twisted micro-flowers for benzaldehyde detection under ultraviolet light excitation

Zichen Zheng [a], Kewei Liu [a,b], Marc Debliquy [b], Chao Zhang [a,*]

[a] College of Mechanical Engineering, Yangzhou University, Yangzhou 225127, PR China
[b] Service de Science des Matériaux, Faculté Polytechnique, Université de Mons, Mons 7000, Belgium

ARTICLE INFO

Keywords:
Gas sensor
Anti-humidity
WO_3/Bi_2WO_6
Benzaldehyde
Carbon cladding

ABSTRACT

Although semiconducting metal oxide displayed remarkable gas sensing capabilities, their path to commercialization is impeded by several challenges. A primary hurdle is the consistent response of sensing films with impervious feature under diverse detection environment. This report introduces an efficient fabrication technique that yields carbon functionalized cladding bismuth tungstate-based benzaldehyde sensors. The 3D twisted micro-flowers feature was obtained and carbon cladding was uniformly attached by a one-pot wet chemistry strategy. The $C_{0.75}/WO_3/Bi_2WO_6$ sensor demonstrates superior sensing capabilities for benzaldehyde at a wide range of detection. It features a remarkable sensitivity (33.7 @ 50 ppm), swift recovery time of 49 seconds, enduring stability exceeding 15 days, and robust selectivity, all at a modest room temperature. Even in conditions of high moisture, the response value exhibited minimal degradation, decreasing by a mere 8.96% compared to its performance in the absence of ambient humidity. The complementary density functional theory calculations suggest that the $C_x/WO_3/Bi_2WO_6$ exhibits a greater benzaldehyde adsorption energy and more robust anti-humidity feature compared to WO_3/Bi_2WO_6, contributing to its enhanced gas-sensing efficacy.

1. Introduction

Benzaldehyde, as a significant volatile organic compound (VOC), is widely used as food additives, plasticizers, low temperature lubricants and cosmetic raw material [1,2]. Nonetheless, as it is a carcinogenic substance with genetic toxicity, which may also cause atopic dermatitis, benzaldehyde has been identified as a hazardous substance [3]. Therefore, many studies have reported the benzaldehyde detection and elimination strategies, including chemiluminescence [4,5], chem-resistive [3,6,7], fluorescence [2], surface plasmon resonance immunosensor [8]. Wang et al. synthetized Co_3O_4-ZnO/rGO composites which can achieve a response of 3–5 ppm benzaldehyde with response and recovery times of 19/12 s [3]. A novel coralloid SnO_2 gas sensor was fabricated by Fang et al., which displayed excellent sensitivity, speedy recovery procedure, and good linear dependence corresponding to benzaldehyde concentration [6]. However, they were still susceptible to environmental influences and limited by low-yield sensitivity and high-power consumption. Hence the progression of exceedingly sensitive and exclusive gas sensor for benzaldehyde detection with moisture-resistant and robust features have to be carried out and improved for scrutinizing food quality and ensuring environmental safety in real-time and on-site.

Among multifarious available strategies, metal oxide semiconductor (MOS) chem-resistive sensors with cost-effective manufacturing, strong sensitivity, uncomplicated layout and high physicochemical stability have been extensively focused [9]. In the specific VOC sensing process, the bulk resistance of MOS is determined by the oxygen adsorption (O_2^-, O^- and O^{2-}) model under temperature dominance [10,11]. In humid environments, chemisorption of water molecules shares the same site on material's surface as adsorption of oxygen species, and electrons acquired by the adsorbed oxygen in this course are returned to the metal oxide, as demonstrated in followed reaction (1) [12]:

$$H_2O + 2M_m + O_{ad}^- \leftrightarrow 2\left(M_m^+ - OH\right) + e^- + S \quad (1)$$

where M refers to metal elements in MOS, including Bi, Sb, and W; M_m represents the site of M on the surface; O_{ad}^- is related to ion-adsorbed oxygen species; e^- refers to the electron; $\left(M_m^+ - OH\right)$ represents a terminal hydroxyl group while S is a surface site for chemically adsorbing oxygen.

When facing with rising humidity as detecting target VOCs, the bond betwixt water molecules with gas-sensitive layers will gradually

* Correspondence to: College of Mechanical Engineering, Yangzhou University, Huayang West Road 196, Yangzhou, Jiangsu Province 225127, PR China.
E-mail address: zhangc@yzu.edu.cn (C. Zhang).

https://doi.org/10.1016/j.snb.2024.135982
Received 17 February 2024; Received in revised form 10 May 2024; Accepted 15 May 2024
Available online 17 May 2024

transform from individual chemisorption to a complex physical and chemical adsorption [13], subsequently the proton hopping manifested will greatly decline the material resistance and the accuracy of sensing in compliance with the Grotthuss mechanism [14], resulting in a greater degree of adsorption competition and deterioration of the sensitivity [15]. In terms of the unsatisfactory and inevitable humidity effect, physical isolation [16], surface engineering [17], novel material development [18], algorism compensation [19], working parameter modulation [20] and other mainstream approaches were adopted to improve the reliability and robustness of ideal sensors. Nonetheless, the predicament existed is that high sensitivity, exclusive detection, low operating temperature and stable output results of gas sensors could not be obtained concurrently. For instance, Kim et al. reported that the Pr-doped $Ce_4W_9O_{33}$-based trimethylamine sensor fabricated by ultrasonic spray pyrolysis method address the water poisoning problem which the sensitivity was barely contingent on the ambient humidity, though preparation process appears time-consuming and expatiatory [21]. Following the idea of loading hydrophobic materials, Sun et al. loaded CuO with the strong affinity to the hydroxyl group on In_2O_3 forming clustered nanospheres to ameliorate moisture resistance detection of CO, yet the selectivity sensing results demonstrated undesirability [22]. Incorporating integrated microheaters with SnO_2/RGOH NO_2 sensors for regulating the working temperature, Wu et al. revealed that the increased temperature will lead to the enhanced immunity to humidity interference [23]. However, the appendant microheater limits the capability of real-time and portable detection while the power consumption is higher. Furthermore, Liu et al. employed 3-aminopropyltriethoxysilane-modified tungsten oxide nanotubes with thin-walled porous features which can provide abundant hydrophobic groups for NO_2 detection, and the sensitivity merely drops to 80% of the incipient response value even in saturated relative humidity [24]. Nevertheless, the above methods still suffered from complex preparation process, insufficient selectivity, intricate detection system, etc. Thus, a breakthrough is urgently needed to develop highly sensitive VOC sensors with reliable sensing performance under high humidity condition.

As WO_3 and Bi_2WO_6 are both n-type semiconductor materials with the appropriate band gap of 2.7–2.9 eV, while they possess high surface activity, effectively adsorbing VOCs in the surrounding environment [25–27]. Furthermore, they both exhibit excellent photocatalytic properties which make them generate electron-hole pairs easily, further enhancing the sensitivity and selectivity towards VOCs under light exposure. The photocatalytic activity also aids in decomposing VOCs adsorbed on the sensor surface, reducing sensor saturation and improving recovery speed [28–30]. Therefore, we introduced D-(+)-Glucose anhydrous as a carbon functionalized cladding for WO_3/Bi_2WO_6 to achieve highly sensitive and robust benzaldehyde detection under room temperature with UV light assistance. Photoexcitation increased the number of carriers with high mobility and reduced the grain boundary barrier, improving the response to benzaldehyde at room temperature [31]. Through combining the carbon-based materials and introducing n-n heterojunctions, the optimal sensing material possessed the stable nanostructure, high specific surface area, abundant surface oxygen vacancy and distinct hydrophobicity. The corresponding sensor exhibited high sensitivity (33.7 @ 50 ppm), robust reproducibility and long-term stability along with distinguishable detection feature. Even at 90% relative humidity (RH), the response value of $C_{0.75}/WO_3/Bi_2WO_6$ sensor declined by only 8.96% relative to the detection scenario without external humidity. Furthermore, the underlying mechanism for high sensitivity and anti-humidity was investigated in relation to the dependence of carbon cladding on MOS nanostructure by density functional theory (DFT) calculation, the configuration of the carbon-modified band structure, and the photoactivated gas-sensing reaction. Finally, the practical application for as-prepared benzaldehyde chem-resistive sensors was explored (Note 7 in Supplementary information). To our knowledge, this report is the inaugural exploration of carbon-clad ternary metal oxide utilized for benzaldehyde detection with anti-humidity sensing analysis, demonstrating the versatility of this MOS sensor.

2. Experimental section

2.1. Chemical reagents

All reagents used were of analytical grade and were utilized without any additional purification. Bismuth nitrate pentahydrate ($Bi(NO_3)_3{\cdot}5\,H_2O$) (AR grade, CAS: 10035–06–0), anhydrous ethanol (AR grade, CAS: 64–17–5) and benzaldehyde (AR grade, CAS: 100–52–7) were acquired from Aladdin Biochemical Technology Co., Ltd. of China. Sodium tungstate dihydrate ($Na_2WO_4{\cdot}2\,H_2O$) (AR grade, CAS: 10213–10–2) and D-(+)-Glucose anhydrous (AR grade, 50–99–7) were obtained from Sinopharm Chemical Reagent Co., Ltd. Polyvinyl pyrrolidone (K30) (AR grade, CAS: 9003–39–8) were purchased from Merck Chemical Technology (Shanghai) Co., LTD.

2.2. Preparation process

Synthesis of C: C were synthesized via a hydrothermal method. Initially, 0.75 g of D-(+)-Glucose anhydrous was dissolved in 60 mL of deionized water. This solution was then transferred to a 100 mL Teflon-lined stainless autoclaves following magnetic stirring for 1 hour. The autoclave was heated to 160 °C and maintained at this temperature for 20 hours before allowing it to cool naturally. The resultant material was isolated by centrifugation with absolute ethanol five times. The final product was dried in an oven at 60 °C for 12 hours.

Synthesis of Bi_2WO_6: Bi_2WO_6 were synthesized via a hydrothermal method which was modified from previous studies [32]. A mixture of 4 mmol of $Bi(NO_3)_3{\cdot}5\,H_2O$, 2 mmol of $Na_2WO_4{\cdot}2\,H_2O$, and 0.6 g of PVP (K30) was prepared in 60 mL of deionized water. This mixture was then transferred to a 100 mL Teflon-lined stainless autoclaves after stirring magnetically for 1 hour. The autoclave was subsequently heated to 160 °C and maintained at this temperature for 20 hours, followed by natural cooling. The products were subjected to centrifugation with absolute ethanol five times. After drying at 60 °C for 12 hours in an oven, the synthesized Bi_2WO_6 were obtained. The final products are referred to as Bi_2WO_6.

Synthesis of $C_x/WO_3/Bi_2WO_6$: $C_x/WO_3/Bi_2WO_6$ were fabricated using an adapted hydrothermal method modified from previous studies (Fig. 1a) [32,33]. In detail, a mixture containing 4 mmol $Bi(NO_3)_3{\cdot}5\,H_2O$, 5 mmol $Na_2WO_4{\cdot}2\,H_2O$, 0.6 g PVP and certain amounts of D-(+)-Glucose anhydrous was prepared in 60 mL of deionized water. This mixture was stirred for 1 hour before being placed into 100 mL Teflon-lined stainless autoclaves. The autoclaves were subjected at 160°C for 20 hours before being allowed to cool to room temperature naturally. The resulting products were isolated by centrifugation using ethanol and deionized water five times and dried at 60°C. The final products synthesized with D-(+)-Glucose anhydrous of 0 g, 0.25 g 0.5 g, 0.75 g, 1 g, 1.5 g and 2 g are denoted as WO_3/Bi_2WO_6, $C_{0.25}/WO_3/Bi_2WO_6$, $C_{0.5}/WO_3/Bi_2WO_6$, $C_{0.75}/WO_3/Bi_2WO_6$, $C_1/WO_3/Bi_2WO_6$, $C_{1.5}/WO_3/Bi_2WO_6$ and $C_2/WO_3/Bi_2WO_6$.

2.3. Characterization

Crystal structures and phases of the samples were characterized using X-ray diffraction (XRD, Bruker D8 Advance) and the micromorphology analysis was elucidated through field emission-scanning electron microscope (FE-SEM, model S4800), transmission electron microscopy (TEM, Tecnai model). Infrared spectral data were acquired using Fourier transform infrared (FTIR) spectroscopy on an Agilent 660-IR, employing the KBr pellet method. The UV-Vis absorption spectra and bandgap were obtained via a UV–vis–NIR spectrophotometer (Cary 5000, Varian, USA). Chemical states of relevant elements and their distribution uniformity were observed via X-ray photoelectron

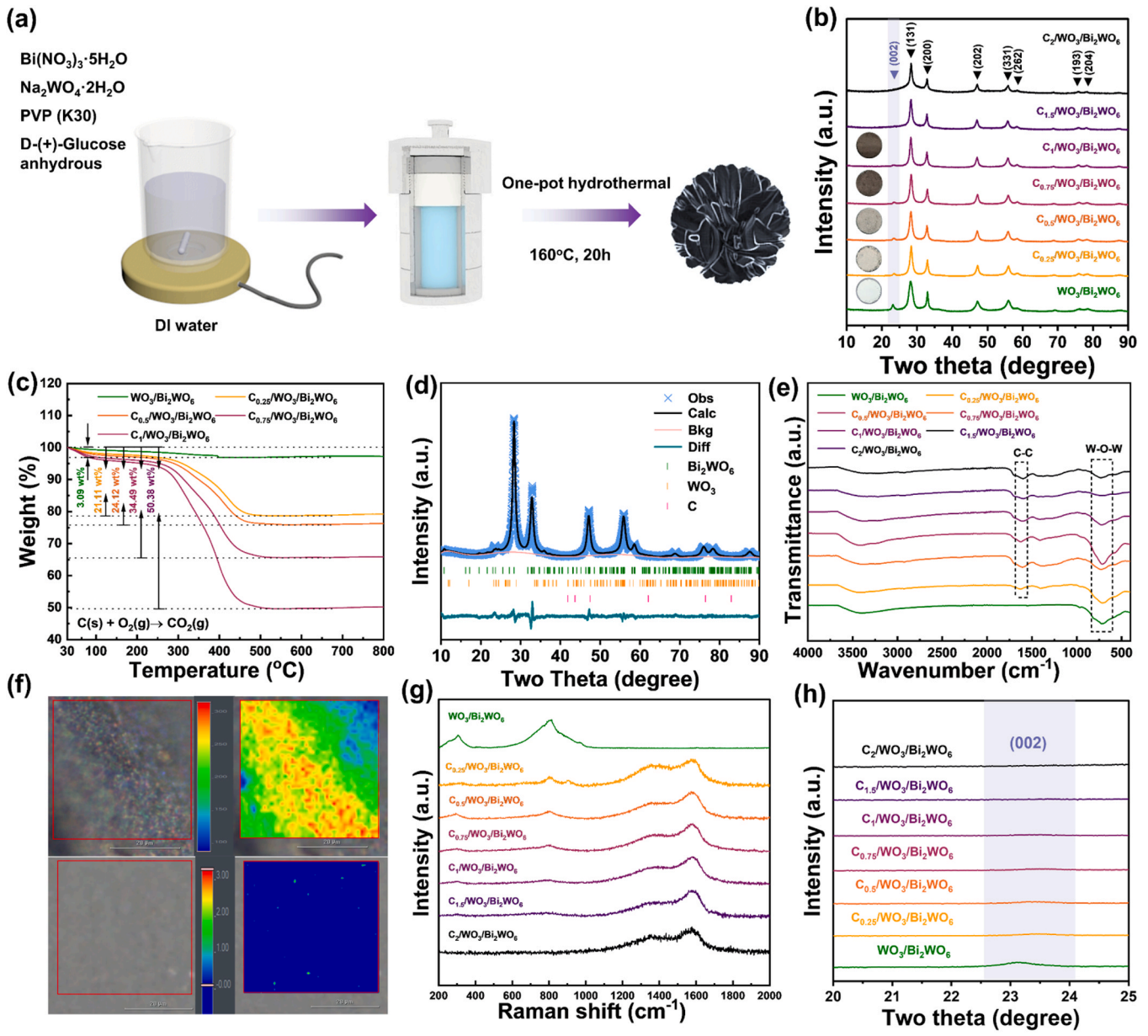

Fig. 1. (a) Schematic illustration for the fabrication of $C_x/WO_3/Bi_2WO_6$, (b) XRD pattern and (c) dynamic TGA curves with a heating rate of 10 °C·min^{-1} of all samples, (d) Rietveld refinement patterns of $C_{0.75}/WO_3/Bi_2WO_6$, (e) FT-IR spectra of all samples; (f) Raman mapping of graphitic G bands in a locally laser-irradiated region of pure WO_3/Bi_2WO_6 (under part) and $C_{0.75}/WO_3/Bi_2WO_6$ (upper part), (g) Raman spectra and (h) magnified portion of XRD pattern (20°-25°) of all samples.

spectroscopy (XPS, Thermo Fisher ESCALAB250Xi) and high-angle annular dark-field scanning transmission electron microscope (HAADFSTEM) with energy dispersive spectroscopy (EDS), respectively. Calibration of the spectrometer was based on the C 1 s peak at 284.8 eV. Electron paramagnetic resonance (EPR, Bruker A300–10/12) was employed to verify the presence of surface oxygen vacancies while the rotational and vibrational mode and Raman mapping images were analyzed by laser confocal Raman spectrometer (Renishaw in Via) and microscopic Raman imaging spectrometer (DXRxi, Thermofisher, USA). Brunauer–Emmett–Teller (BET) surface area with N_2 adsorption/desorption isotherms and pore-size distribution was investigated via specific surface and aperture analyzer (Autosorb IQ3, Quantachrome Instruments). The mass variation as a function of temperature during the heating process was studied through Thermogravimetric (TGA) analysis (Pyris 1 TGA, PerkinElmer, USA). Water contact angle (WCA) measurements were conducted using a LAUDA Scientific GmbH LAUDA OSA 100 system to assess surface hydrophobicity.

XRD with a Cu-Kα anode source (λ=0.15406 nm) was operated at 40 kV voltage and 40 mA current with the scanning step of 5°/min. HRTEM and SAED operated at 200 kV accelerating voltage, and the interplanar spacing was analyzed via Gatan Digital Micrograph software. All of the binding energies of XPS analysis with monochromatic Al-Kα radiation were calibrated by the signal of carbon C 1 s peak with a binding energy of 284.8 eV. FTIR spectra were recorded using the KBr pellets method on infrared spectrophotometer with a resolution of 0.1 cm^{-1} in the range of 4000–400 cm^{-1}. The BET and pore size distributions were obtained from nitrogen physisorption isotherms acquired at 77 K. The TGA analysis was performed from 30 °C to 800 °C in N_2 with a hating rate of 10 °C/min.

2.4. Gas sensor fabrication and measurements

Initially, the target solutions were obtained by uniformly mixing 3 mg of $C_x/WO_3/Bi_2WO_6$ powders with 1 mL of absolute ethyl alcohol.

This mixture was uniformly coated onto an Al_2O_3 substrate equipped with interdigital Pt electrodes. Subsequently, the sensors were subjected to an aging process at 120 °C for 24 hours. Gas-sensing tests were performed using a four-channel gas sensing tester. The testing apparatus consists of two main components: an air intake system and a detection unit. Synthetic dry air (79% N_2 + 21% O_2) was sourced from Nanjing Special Gas Factory Co., Ltd. The four-channel gas sensing tester was acquired from Wuhan Huachuang Ruike Technology Co., LTD. To adjust the concentration of benzaldehyde, mass flow controllers from Bronkhorst, Germany, were used to vary the flow rates of the synthetic dry air. This instrument measures the electrical resistance changes in both high-purity air and the specific VOCs over time, detailing the resistance variation pattern. All tests were performed at room temperature (25 ± 2 °C) and the mean relative humidity was approximately 15–20% without any additional moisture control. The power of UV irradicated at the surface of sensor is 1.0 mW/cm^2. A desktop computer was employed to collect response data equipped with an analog to digital (A/D) data acquisition board that gathers electrical resistance values of the corresponding channels with a laboratory DC power supply (GPS-3303 C) of 12 V and 4 A. In detail, the data logger supplies a steady voltage of 2.5 V (V_{EX}). This voltage is distributed between the reference resistor (R_{ref}), which has a known and constant resistance, and the IDA-CR, whose resistance changes according to the detected benzaldehyde concentration. The voltage is relatively distributed according to the resistance of the two circuit components. Therefore, given the voltage between V_{EX} and ground (GND), the voltage between V_{meas} and GND is measurable, and from their ratio, it is possible to calculate IDA-CR resistance, as described in Eq. (2).

$$\frac{V_{meas}}{V_{EX}} = \frac{R_{CR}}{R_{CR} + R_{ref}} \rightarrow R_{CR} = \frac{R_{ref} \bullet \left(\frac{V_{meas}}{V_{EX}}\right)}{1 - \left(\frac{V_{meas}}{V_{EX}}\right)} \quad (2)$$

The benzaldehyde vapor with a certain concentration was obtained via a simple dynamic gas distribution method. The saturated vapor pressures of benzaldehyde liquids are 0.13 kPa or 0.975 mmHg (26 °C). The flow (x, unit: sccm) of standard benzaldehyde with the concentration of 1282.997 ppm was calculated by Eq. (3) [34] and controlled with one mass flow controller. The standard octanal, 2-pentylfuran, nonanal, 1-octen-3-ol, hexanal and 1-octanol with the saturated vapor pressures of 2.1014 mmHg, 2.0216 mmHg, 0.2584 mmHg, 0.8284 mmHg, 10.488 mmHg and 0.1406 mmHg were calculated to be 2765 ppm, 2660 ppm, 340 ppm, 1090 ppm, 13800 ppm and 185 ppm, respectively at room temperature by Eq. (3) as well. The standard ethanol with the concentration of 2000 ppm was obtained from Nanjing Special Gas Factory Co., Ltd. The flows of dry air (y, in sccm) and humid air (z, in sccm) from high purity mixed air were managed using two mass flow controllers. The concentrations of VOCs (expressed in ppm) were calculated as 100x/(x+y+z) by independently managing the flows. Relative humidity was regulated using two distinct flow meters; one for dry air (flow rate: A sccm) and another for fully humidified air (flow rate: B sccm). The relative humidity was determined by the formula B/(A+B)*100%.

$$\text{Concentration of VOCs (ppm)} = (\text{vapor pressure of VOCs (mmHg)}/760) \times 10^6 \quad (3)$$

The sensor response is expressed as R_a/R_g, where R_a and R_g denote the resistance in the presence of air and the target gas, respectively. The response and recovery time indicated the time needed for the resistance to change by 90% during the exposure and removal stages of the target gas, respectively.

3. Results and discussion

3.1. Morphology and structure characterization

The highly anti-humidity and exclusive $C_x/WO_3/Bi_2WO_6$ chemo-resistive sensors were prepared by a elementary, one-step roadmap (Preparation process section and Fig. 1a). Distinctively, PVP (K30) serves both as a stabilizer and a crystallization inhibitor, preventing ionic aggregation during the reaction process and controlling the size and morphology of bismuth tungstate and tungsten oxide, ensuring their uniformity in shape. Thus, simultaneously under the action of PVP dispersant, D-(+)-Glucose anhydrous can form a uniform carbon coating naturally. All the diffraction peaks of the Bi_2WO_6 pattern were matched to the cubic phase (JCPDS Card No. 39–0256) and the WO_3 was indexed to the cubic phase (JCPDS Card No. 52–8916) (Fig. 1b, Fig. S1). As the amount of D-(+)-Glucose anhydrous increases gradually, the color of the samples progressively deepened and the intensity of characteristic peak of WO_3, (002), decreases slowly and eventually disappears (Fig. 1h), demonstrating an excess of D-(+)-Glucose anhydrous would lead to the destruction of WO_3/Bi_2WO_6 double heterojunction, degrade the positive role of PVP. The texture coefficient values of seven samples were calculated (Table S2 and Fig. S10) [35] and the corresponding value of each crystallographic plane displayed no evident variation, manifesting the C cladding may not lead to re-orientation effect. Meanwhile, the pure carbon was synthesized via the one-step hydrothermal strategy above and the C exists in two forms: as nanoparticles and as micrometer-sized spheres (Fig. S2). To verify the successfully functionalization of caron cladding, we performed TGA characterization on five typical samples, and the results demonstrated that with the augment of D-(+)-Glucose anhydrous addition, the mass of the samples decreased further correspondingly (From WO_3/Bi_2WO_6 to $C_1/WO_3/Bi_2WO_6$: 3.09 wt%, 21.11 wt%, 24.12 wt%, 34.49 wt%, 50.38 wt%), while carbon will be converted into CO_2 during this process. To gain a more comprehensive insight into the crystal structure of as-prepared products, the XRD Rietveld refinement analysis was carried out as depicted in Fig. 1d and Fig. S3-S9. The analysis of $C_{0.75}/WO_3/Bi_2WO_6$ yielded a notably low weighted residual (R_{wp} = 8.444%), manifesting a high degree of correlation between the refined pattern and the original XRD observations. As show in Fig. 1e, we discerned the peak located at approximately 719 cm^{-1} was correlated to W-O-W bond [36,37] while the peak at 1618 cm^{-1} was matched to the ring C-C stretch [38], which verify the smoothly encapsulation of the carbon. Furthermore, the most intense W-O-W peak was observed in sample $C_{0.75}/WO_3/Bi_2WO_6$, revealing the higher concentration of specific molecules that absorbed photons in the sample, which was beneficial to enhance the sensitivity. Finally, the Raman spectrum of all samples and Raman mapping of WO_3/Bi_2WO_6 and $C_{0.75}/WO_3/Bi_2WO_6$ were conducted (Fig. 1f and Fig. 1g). Additionally, the relative weak peak observed at around 1362 cm^{-1} correlates with the defeats and disordered structure of the carbon portion (D band), while the relative strong peak at approximately 1573 cm^{-1} is indicative of the planar vibration mode characteristic of sp^2-hybridized carbon atoms (G band) [39], which further confirming the successful formation of C cladding. As shown in Fig. 1f, the Raman mapping of G band (1573 cm^{-1}) and D band (1362 cm^{-1}) of $C_{0.75}/WO_3/Bi_2WO_6$ presented high intensity which verified the uniform distribution of C and the existentially induced defects. Furthermore, the C is in the compressed state in the green region and constringent C-C bond is owing to the hydrothermal reaction at high temperature [40], verifying it's robust and anti-humidity feature while the procreant defect states will facilitate the absorption of UV light, enhancing gas sensing performance.

Via regulating the amount of D-(+)-Glucose anhydrous, adequate C were clad on the appointed heterojunction, thus $C_{0.75}/WO_3/Bi_2WO_6$ with the 3D twisted micro-flower nature was prepared (Fig. 2a and Fig. 2b). In detail, it was assembled by abundant mesoporous WO_3/Bi_2WO_6 with C cladding branches rotating around a specific axis. PVP

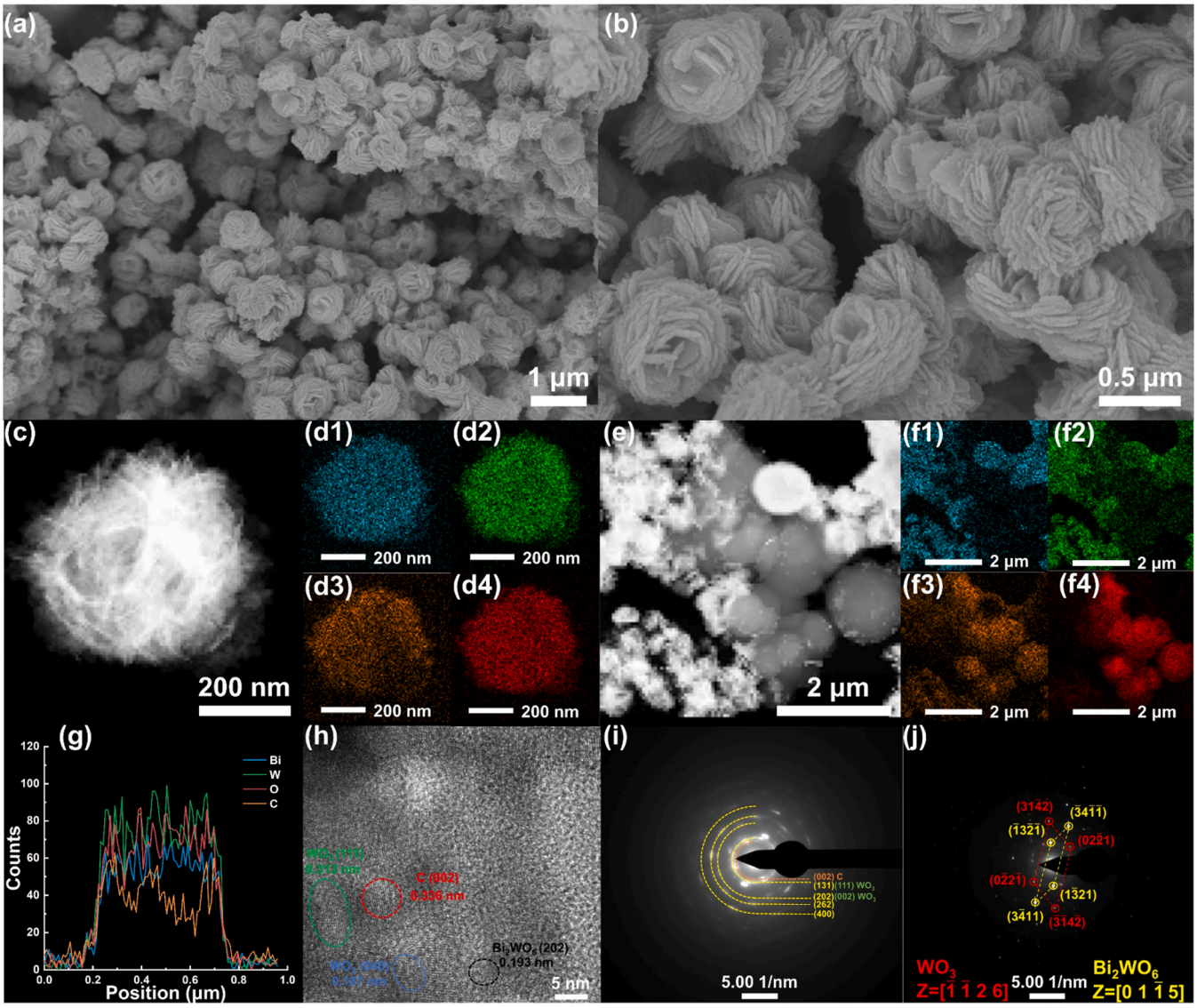

Fig. 2. (a-b) FESEM image of $C_{0.75}/WO_3/Bi_2WO_6$ shows its 3D twisted micro-flower nature, (c-d) EDS elemental mapping results of $C_{0.75}/WO_3/Bi_2WO_6$ in two different perspectives (d1: Bi, d2: W, d3: O, d4: C), (e-f) EDS elemental mapping results of $C_{1.5}/WO_3/Bi_2WO_6$ in two different perspectives (f1: Bi, f2: W, f3: O, f4: C), (g) EDS linear scanning results of $C_{0.75}/WO_3/Bi_2WO_6$, (h) high-resolution TEM images of $C_{0.75}/WO_3/Bi_2WO_6$, SAED analysis of (i) $C_{0.75}/WO_3/Bi_2WO_6$ and (j) WO_3/Bi_2WO_6.

acts as a dispersant in the synthesis to prevent the aggregation of bismuth, tungsten and carbon sources, facilitating the acquisition of uniform $C_{0.75}/WO_3/Bi_2WO_6$ micro-flower. The morphology of other samples was also examined (Fig. S11) while the atomic weight ratios and atomic ratios of Bi, W, O and C in samples through EDS spectra were depicted in Fig. S12 and Fig. S13, which illustrating the incremental C content with the increase adding of D-(+)-Glucose anhydrous content. However, there exists a singular point that the atom ratio of C of $C_{0.75}/WO_3/Bi_2WO_6$ is higher than that of $C_1/WO_3/Bi_2WO_6$, which may be by reason of the synergistic effect of appropriate D-(+)-Glucose anhydrous adding content and PVP stabilizer resulting in a slightly higher C content in $C_{0.75}/WO_3/Bi_2WO_6$ sample. Furthermore, the high-resolution TEM (HRTEM) was implemented for $C_{0.75}/WO_3/Bi_2WO_6$ (Fig. 2c-2d) and $C_{1.5}/WO_3/Bi_2WO_6$ (Figs. 2e-2f). Bi (Fig. d1), W (Fig. d2), O (Fig. d3) and C (Fig. d4) were distributed uniformly over the whole 3D $C_{0.75}/WO_3/Bi_2WO_6$ twisted micro-flower, while the EDS linear scanning results confirm this viewpoint simultaneously (Fig. 2 g and Fig. S14). Expressly, as shown in Fig. 2c of high-angle annular dark-field images (HAADF) about $C_{0.75}/WO_3/Bi_2WO_6$, there exists bight and dark areas intermingled together, proving that it owned a certain hollow property and possessed erythrocyte-structure. In detail, the thickness of $C_{0.75}/WO_3/Bi_2WO_6$ 3D micro-flowers increases with the augment of the diameter from the axis outward. However, there still leaves a large amount of C in the form of spheres in $C_{1.5}/WO_3/Bi_2WO_6$ samples (Fig. 2e and Fig. 2 f), indicating the importance of adding appropriate amount of D-(+)-Glucose anhydrous. Three categories of clear lattice fringes for Bi_2WO_6, WO_3 and C of $C_{0.75}/WO_3/Bi_2WO_6$ were marked thoroughly (Fig. 2 h, Fig. S15a-15b). In detail, the lattice spacing of 0.390 nm, 0.301 nm and 0.218 nm was corresponding to the (002), (111) and (220) plane (Fig. S15c2) of WO_3, respectively. As for Bi_2WO_6, the metrical space between contiguous lattice fringes were 0.314 nm, 0.196 nm and 0.157 nm, which can be assigned to exemplary plane of (131), (202) (Fig. S15c1 and Fig. S16c) and (262), respectively. The interplanar spacing of 0.34 nm along two orthogonal directions are corresponding with the (020) crystallographic plane of carbon (Fig. S15c3 and Fig. S16a) [41]. The post-optimized FFT images of $C_{0.75}/WO_3/Bi_2WO_6$ for Bi_2WO_6 (Fig. S16d) and C (Fig. S16b) were obtained which verifying the veracity of measured spacing of lattice

fringes. Meanwhile, the selected area electron diffraction (SAED) for $C_{0.75}/WO_3/Bi_2WO_6$ was examined (Fig. 2i), demonstrating the polycrystalline property itself, as the distinctly visible diffraction rings with a small number of spots can be discerned, which is in accordance with the XRD analysis. In addition, the SAED experiments for WO_3/Bi_2WO_6 were carried out as well (Fig. 2j). The monocrystal feature of WO_3/Bi_2WO_6 without C cladding was discerned.

The X-ray photoelectron spectroscopy (XPS) analysis is employed to ascertain the surface elemental composition and chemical state of the samples synthesized. Low resolution survey unveils the core level peaks of Bi 5d, Bi 4 f, Bi 4p, W 4d, W 4 f, O 1 s, and C 1 s of all prepared samples (Fig. 3a). The C 1 s spectra of $C_{0.75}/WO_3/Bi_2WO_6$ can be deconvoluted into four peaks located at 288.44 eV, 286.82 eV, 285.47 eV and 284.42 eV which are assigned to O═C-O, C═O, C-O and C-C, respectively [42,43], which verifying the fulfillment of C cladding. As depicted in Fig. 3c, the O 1 s spectra of $C_{0.75}/WO_3/Bi_2WO_6$ and WO_3/Bi_2WO_6 was deconvoluted into surface-chemisorbed oxygen (O_C), oxygen vacancies (O_V) and lattice oxygen (O_L). After C cladding, the binding energy of O_V and O_L experienced an increase, which can be attributed to the relatively diminutive electronegativity disparity between C and O compared to that of Bi/W and O, leading to the formation of covalent bonds. Consequently, the peaks associated with O_V and O_L were shifted towards higher binding energies due to the bonding of O with both C, BI and W. Furthermore, the highest percentage of O_V (44.25%) and O_C (23.56%) of $C_{0.75}/WO_3/Bi_2WO_6$ was calculated (Fig. 3f), which enhanced the sensing performance at a deep level, while it is mainly reflected in the regulation of the sensor baseline resistance and O_V distribution [44]. Meanwhile, the higher concentration of O_C increases the oxidation reaction rate and signal output, reduces the noise interference, comprehensively improves the stability of $C_{0.75}/WO_3/Bi_2WO_6$ sensor. In the case of W 4 f spectra for $C_{0.75}/WO_3/Bi_2WO_6$ sample (Fig. 3d), it was deconvoluted into W 4 $f_{5/2}$ and W 4 $f_{7/2}$ centered at 37.5 eV and 35.3 eV, which are higher 0.2 eV than that of WO_3/Bi_2WO_6. Meanwhile, the Bi 4 f spectra of $C_{0.75}/WO_3/Bi_2WO_6$ can be divided into Bi 4 $f_{5/2}$ and Bi 4 $f_{7/2}$ peaks which are observed at 164.4 eV and 159.1 eV, while 0.2 eV decline was discerned compared to the sample without C cladding (Fig. 3e) [25]. The red shift of W 4 f and Bi 4 f spectrum demonstrated the low binding energy and high electron cloud density of $C_{0.75}/WO_3/Bi_2WO_6$, stimulating the adsorption and desorption rates of oxygen species and target gases. In addition, the high-resolution survey for other samples are depicted at Fig. S17-S20.

To investigate the impact of C cladding on the formation of O_V, EPR measurements were conducted on all samples as shown in Fig. 3g. All samples displayed a symmetrical EPR signal at g=2.003. The highest signal intensity and intensity ratio (Fig. 3h) of $C_{0.75}/WO_3/Bi_2WO_6$

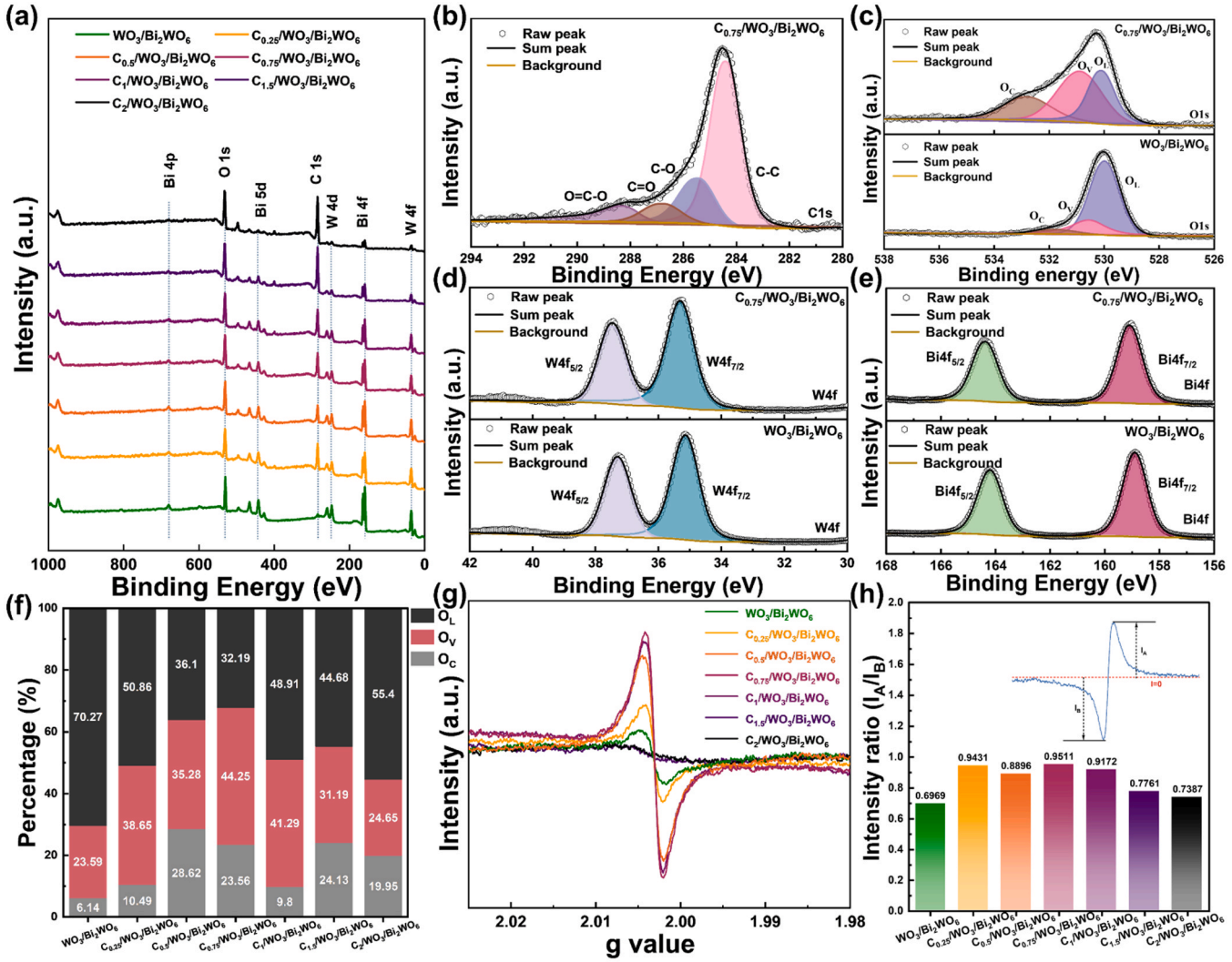

Fig. 3. XPS spectra of the samples: (a) Low resolution survey and (b) high-resolution C 1 s of $C_{0.75}/WO_3/Bi_2WO_6$; high-resolution (c) O 1 s; (d) W 4 f and (e) Bi 4 f of $C_{0.75}/WO_3/Bi_2WO_6$ and pure WO_3/Bi_2WO_6. (f) oxygen species proportion and (g) EPR spectra of samples, (h) Intensity ratio of symmetry parameters of defect signal. Inset: the ratio of symmetry coefficients is defined as I_A/I_B.

illustrated that $C_{0.75}/WO_3/Bi_2WO_6$ possessed the highest concentration and the most evenly distributed O_V [45], which is in superb agreement with the XPS results. Furthermore, the UV–vis and BET analysis were added in Note 1.

3.2. Sensing properties of gas sensors

Due to the high photon energy generated by the visible light, which would produce more electron-hole pairs, degrading the sensing process [30]. The UV light (365 nm) was selected as the excitation source to facilitate the charge modulation and weaken the excitonic effects [46]. We obtained the responses variation curves of $C_{0.75}/WO_3/Bi_2WO_6$ gas sensor towards benzaldehyde (40–4 ppm) under UV light irradiation with the intensity at 1.0 mW/cm^2 and dark conditions (Fig. S22). Compared with the two situations, $C_{0.75}/WO_3/Bi_2WO_6$ exhibited improved sensing performance while the response value was increased by more than 2 times, which was attributed to the increased generation of photocarriers facilitated by UV excitation in the $C_{0.75}/WO_3/Bi_2WO_6$ twisted micro-flowers, which in turn strengthen the density of electrons and active sites on the surface, allowing them to participate in the sensing reaction [47]. Furthermore, to comprehend the impact of photo-assisted activation on gas detection process, a comparative analysis of I-V characteristics for the $C_{0.75}/WO_3/Bi_2WO_6$ sensor was conducted between conditions of darkness and exposure to UV light (Fig. S23). Compared to dark condition (e.g., 0.010 mA at 4 V), the 4 V current increased to 0.034 mA under UV light irradiation, which allowing the $C_{0.75}/WO_3/Bi_2WO_6$ sensor resistance to be measured easily. The triple augment in current observed upon UV light exposure clearly signifies the photo-induced generation of charge carriers within the $C_{0.75}/WO_3/Bi_2WO_6$ sensor [9]. Therefore, the following gas sensing experiments were carried out under the condition of UV light excitation. The dynamic transient response curves of as-prepared samples toward 125–25 ppm benzaldehyde were obtained while $C_{0.75}/WO_3/Bi_2WO_6$ exhibited the highest sensitivity (160.5@125 ppm) (Fig. 4a). Furthermore, the $C_{0.75}/WO_3/Bi_2WO_6$ and $C_1/WO_3/Bi_2WO_6$ still exhibited the high response of 7.2 and 6.1 at low benzaldehyde concentration of 25 ppm (Fig. 4b). The response of gas sensor first increased and then decreased with the augment of carbon cladding content, while the

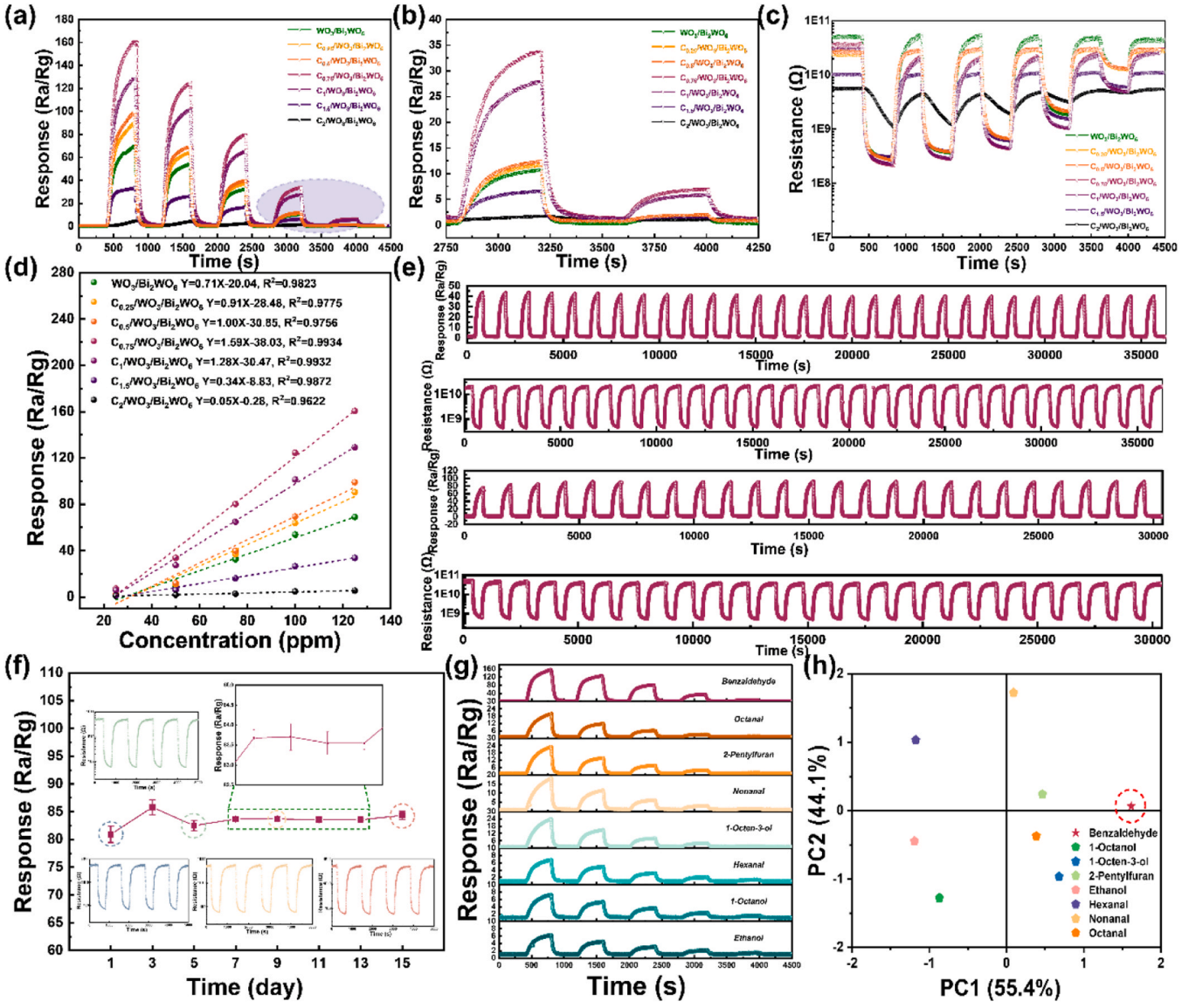

Fig. 4. (a) Transient response of $C_x/WO_3/Bi_2WO_6$ film to benzaldehyde concentrations of 25–125 ppm, (b) magnified area of Fig. 4(a), (c) resistive response of $C_x/WO_3/Bi_2WO_6$ gas sensors toward exposure to 25–125 ppm of benzaldehyde, (d) concentration-dependent response curves of the $C_x/WO_3/Bi_2WO_6$-based sensor for benzaldehyde, (e) repeatability of the $C_{0.75}/WO_3/Bi_2WO_6$ sensor under 50 and 80 ppm benzaldehyde, (f) long-term stability of the $C_{0.75}/WO_3/Bi_2WO_6$ gas sensor to 75 ppm formaldehyde, (g) transient response, (h) pattern recognition by the PCA method to analyze the selectivity of the $C_{0.75}/WO_3/Bi_2WO_6$-based sensor.

corresponding reference resistance consistently declined (Fig. 4c), proving that the narrowed bandgap formation and impurity scattering reduction. Also, on the basis of Fig. 4d, all the sensors possessed the outstanding linearity over a wide detection range. The profoundly reproducible sensing feature under repetitive thirty cycles of $C_{0.75}/WO_3/Bi_2WO_6$ sensor was obtained (Fig. 4e), while the sensor platform also displayed excellently robust environmental long-term stability for 15 days (Fig. 4f). The discriminative benzaldehyde detection and analysis was meticulously revealed in Fig. 4g and Fig. S24. Firstly, the dynamic response curves of $C_{0.75}/WO_3/Bi_2WO_6$ sensor to 8 diverse VOCs (25–125 ppm) were acquired while the highest sensitivity for benzaldehyde can be discerned (Fig. 4g). The specific response value and response time of $C_{0.75}/WO_3/Bi_2WO_6$ sensor platform for discriminative detection were listed at Table S4-S6). The Eley-Rideal model is utilized for investigating the kinetic properties involved in benzaldehyde and interfering gas sensing, and the derived parameters can be subsequently employed to differentiate VOCs by principal component analysis (PCA) patterns [48]. We could obtain the sensitivity (η), kinetic reaction rate constant (κ_r), β value and activation energy (E_a) from Fig. S24a-24d and the concrete analysis procedure was demonstrated in Note 3 and Table S7. As a extensively used statistical method, PCA is capable of transforming a collection of potentially interrelated variables

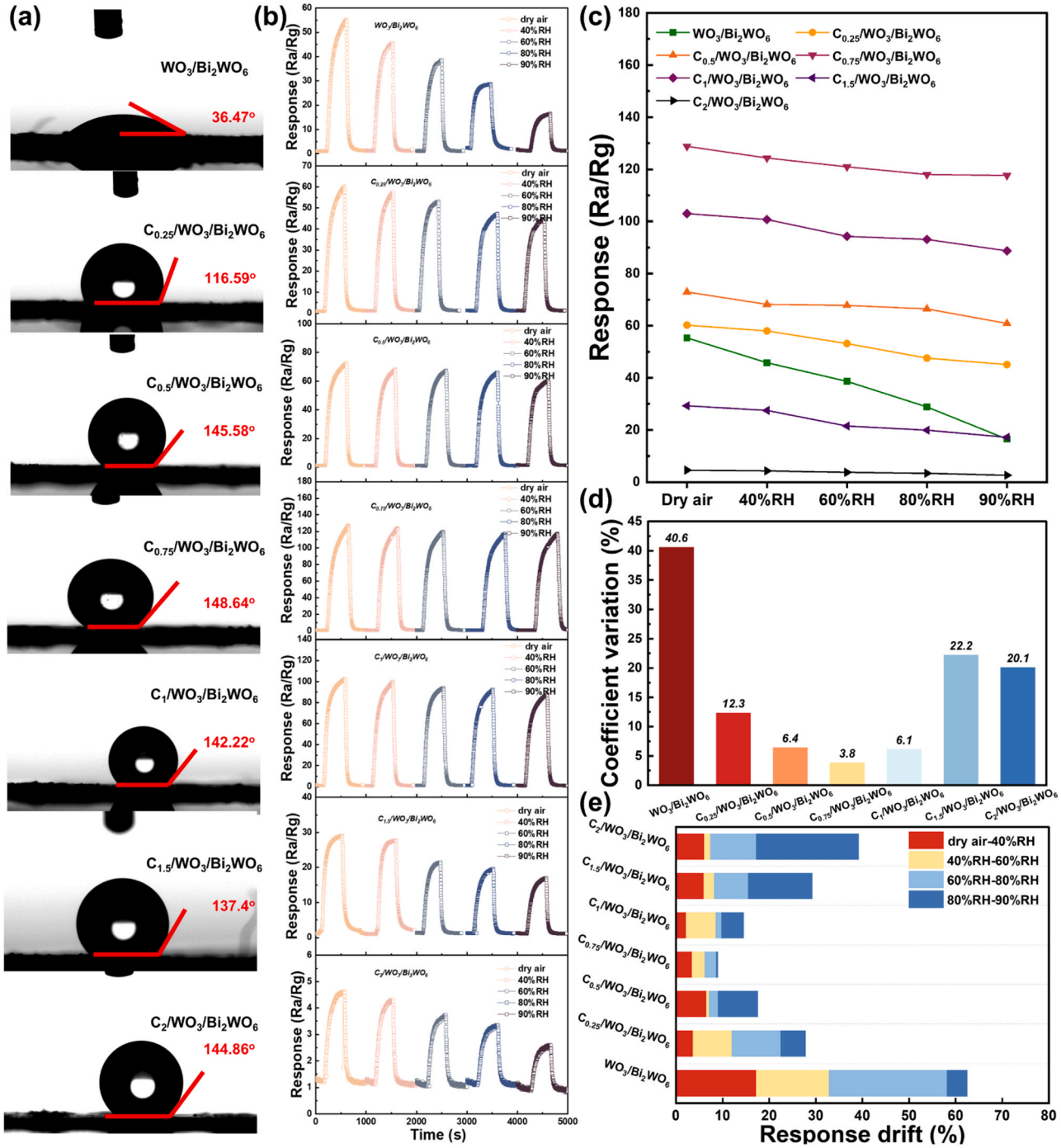

Fig. 5. (a) Water contact angle of all sample films, (b) transient response of all sample films to benzaldehyde concentrations of 100 ppm under dry air circumstance, 40%RH, 60%RH, 80%RH and 90%RH at room temperature (25 ± 2 °C), (c) plots of response retentions for different sensors as a function of RH, (d) CV values of different sensors, (e) response drift of different sensors.

into a set of linearly uncorrelated variables through an orthogonal transformation process [49]. The kinetic parameters to diverse VOCs were set as input data. The resulting score plot displayed a beneficial separation and distinction of benzaldehyde point among 8 analytes, further confirming the excellent exclusive sensing performance of $C_{0.75}/WO_3/Bi_2WO_6$ sensor (Fig. 4h).

The carbon cladding functionalizing can incredibly alleviate the influence of ambient humidity on chem-resistive bismuth tungstate sensor operation as the intrinsically hydrophobic of C film which can potentially reduce the reaction between the sensing layer and H_2O. The WCA of WO_3/Bi_2WO_6 and $C_x/WO_3/Bi_2WO_6$ films were illustrated (Fig. 5a). The WCA of the WO_3/Bi_2WO_6 film is merely 36.47°, demonstrating its hydrophilic characteristics. In particular, the addition of a small amount of D-(+)-Glucose anhydrous (0.25 g) will provide the $C_{0.25}/WO_3/Bi_2WO_6$ with hydrophobic feature and the corresponding WCA is 116.59°. Furthermore, the WCA of $C_x/WO_3/Bi_2WO_6$ (x= 0.5, 0.75, 1, 1.5 and 2) were all greater than 130°, which proved the C cladding can be served as hydrophobic film for humidity-alleviation benzaldehyde detection. The dynamic response curve of all samples to 100 ppm benzaldehyde under dry air circumstance and RH in the range of 40–90% under UV light (365 nm) excitation were depicted as Fig. 5b while the relevant response values were consolidated into Fig. 5c. The WO_3/Bi_2WO_6-based sensor's sensitivity was significantly affected by atmospheric humidity (green portion), resulting in substantial drift in the response value as humidity levels increased (Fig. 5e). The concrete response value for WO_3/Bi_2WO_6 sensor was 45.22% (40%RH~90%RH) while the equivalent value for $C_{0.75}/WO_3/Bi_2WO_6$ 5.49% in the same circumstance. Furthermore, we applied the coefficient of variation (CV) to demonstrate the impact of humidity on responses (Fig. 5d), which is defined as Eq. (4) [50]:

$$CV = R_{SD}/R_{average} \times 100\% \quad (4)$$

where R_{SD} and $R_{average}$ represent the standard deviation (SD) while the average value of responses obtained under varying humidity conditions, respectively. The CVs of the WO_3/Bi_2WO_6 to $C_2/WO_3/Bi_2WO_6$ was 40.6, 12.3, 6.4, 3.8, 6.1, 22.2 and 20.1, respectively. As the CVs value was negatively correlated with the moisture resistance of the material, adding between 0.5 and 1 g of D-(+)-Glucose anhydrous can improve

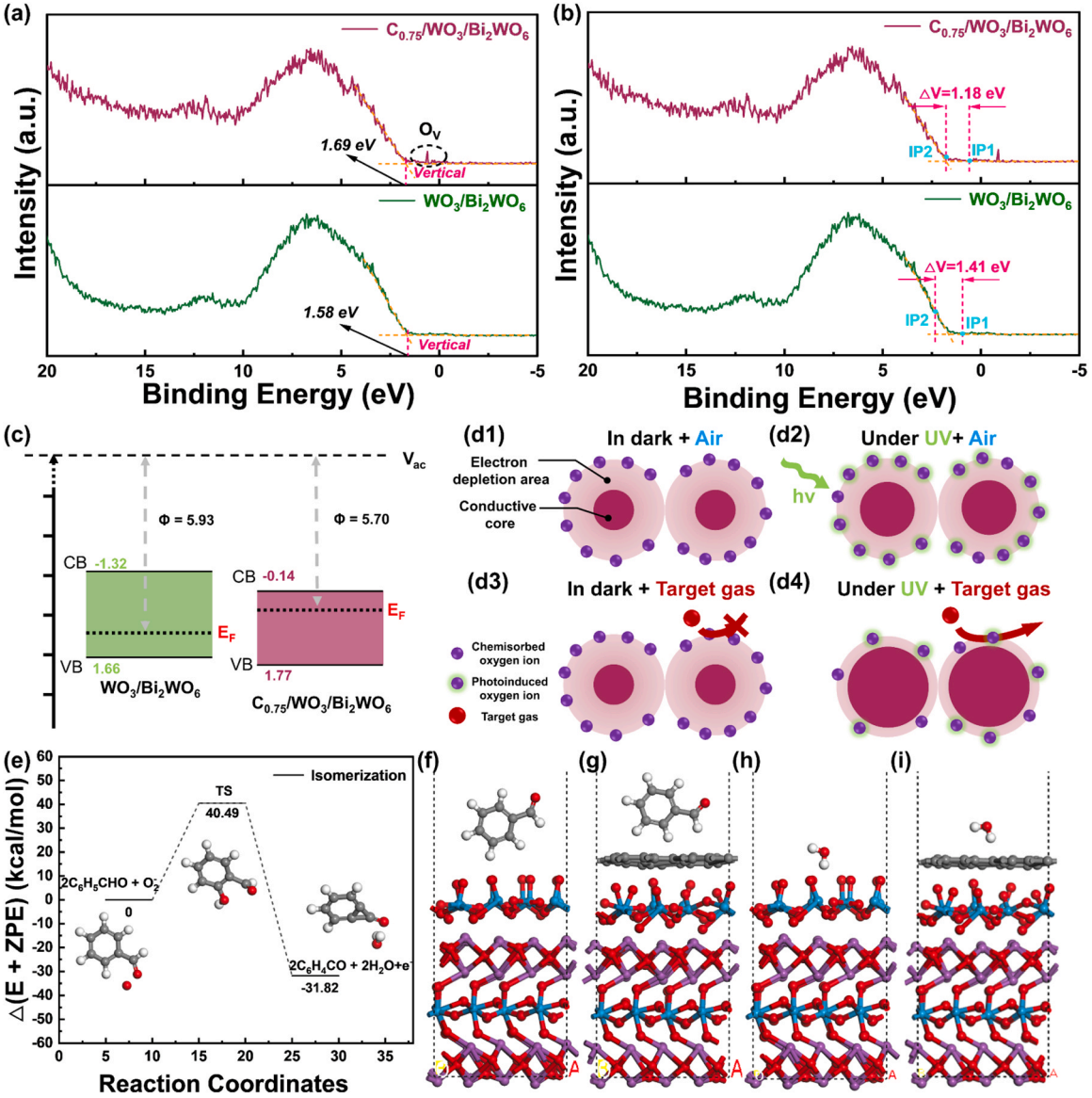

Fig. 6. (a) VB-XPS, (b) work functions and (c) band structure of $C_{0.75}/WO_3/Bi_2WO_6$ and WO_3/Bi_2WO_6, (d1-d4) Schematic illustration of mechanism of photo-assisted gas sensing under UV excitation, (e) the reaction path of benzaldehyde during sensing, optimized structures for benzaldehyde adsorption in (f) WO_3/Bi_2WO_6 and (g) $C_{0.75}/WO_3/Bi_2WO_6$, Optimized structures for H_2O adsorption in (h) WO_3/Bi_2WO_6 and (i) $C_{0.75}/WO_3/Bi_2WO_6$.

the anti-humidity ability of $C_x/WO_3/Bi_2WO_6$ to the maximum extent.

3.3. Gas sensing mechanism

At present, the VOC sensing mechanism was comprehensively studied and the fundamental benzaldehyde sensing process for $C_x/WO_3/Bi_2WO_6$ can be interpreted as the oxidation-reduction reaction between ionized oxygen species (O_2^-, O^- and O^{2-}) and benzaldehyde molecules, which can be referred to our previous study [35, 51–53]. Based on the above results, it was conjectured that the strengthened benzaldehyde sensing performance were ascribed to the carbon functionalized cladding, n-n heterostructure setting up, optical excitation and optimized twisted micro-flowers morphology. Firstly, the n-n heterojunction formed by tungsten oxide and bismuth tungstate contributed to the internal electric field construction and can reduce the reference resistance, decreasing the power consumption. Secondly, the band structure of $C_{0.75}/WO_3/Bi_2WO_6$ and WO_3/Bi_2WO_6 can be obtained by VB-XPS and Tauc plots (Figs. 6a-6c, Note 1 and 4). As shown in Fig. 6a, there exists a characteristic peak of O_V near valence band, verifying the higher concentration of O_V in $C_{0.75}/WO_3/Bi_2WO_6$, which is consistent with the EPR and O 1 s results [54]. Furthermore, the higher work function of $C_{0.75}/WO_3/Bi_2WO_6$ can be discerned (Fig. 6c), demonstrating the lower baseline resistance, stronger built-in electric field and faster reactive electron transfer rate were acquired. Thirdly, the reason for the enhanced sensitivity of $C_x/WO_3/Bi_2WO_6$ sensor from UV light excitation is the chemically adsorbed oxygen ions ($O_{2(ads)}^-$) on the surface of $C_x/WO_3/Bi_2WO_6$ is greatly stable under dark conditions while the larger adsorption energy between $C_x/WO_3/Bi_2WO_6$ and $O_{2(ads)}^-$ will result in the nonspontaneous O_2^- desorption. However, the electrons induced by photo-excitation will continue to react with O_2 to form more oxygen species ($O_{2(photo\text{-}ads)}^-$) under ultraviolet light, making its desorption process easier above $C_x/WO_3/Bi_2WO_6$ surface (Fig. 6d). Unlike $O_{2(ads)}^-$, $O_{2(photo\text{-}ads)}^-$ are relatively feeble bound to the surface of $C_x/WO_3/Bi_2WO_6$, which can react with benzaldehyde molecules rather spontaneously, leading to prominent resistance change (Fig. S22) [9]. Following the successful incorporation of carbon, the gas sensing activity and stability for $C_x/WO_3/Bi_2WO_6$ have been improved as the excitons have been dissociated into free carriers, alleviating the side effects of photoexcitation [44]. Meanwhile, carbon could facilitate the carrier mobility rate while the existed electron transfer procedure ($Bi/W \rightarrow C_{Bi/W} \rightarrow C_O \rightarrow O$) may provide novel carrier transport channels, acquiring the greater reactivity and rapider reaction. Furthermore, the concrete reaction of benzaldehyde molecule was illustrated in Fig. 6e and Eqs. (5–7) [55,56]:

$$O_{2(gas)} \leftrightarrow O_{2(ads)} \tag{5}$$

$$O_{2(ads)} + e^- \leftrightarrow O_{2(ads)}^-(T < 150^oC) \tag{6}$$

$$2C_6H_5CHO_{(gas)} + O_{2(ads)}^- \rightarrow 2C_6H_4CHO_{(gas)} + 2H_2O + e^- \tag{7}$$

Finally, the DFT results confirmed that the adsorption energy of benzaldehyde on carbon is higher (-1.795 eV) (Fig. 6g), which is about three times that of the adsorption energy on the surface of WO_3/Bi_2WO_6 (-0.614 eV) (Fig. 6f), proving that C cladding is beneficial to the improvement of sensitivity of the sensor. Furthermore, the adsorption energy of water molecule to optimized geometric construction of $C_x/WO_3/Bi_2WO_6$ and WO_3/Bi_2WO_6 was −0.256 eV and −0.793 eV, respectively (Figs. 6h-6i), which is consistent with the actual sensing results in part 3.3 (Fig. 5). On the whole, carbon materials (such as graphene, carbon nanotubes, activated carbon, etc.) typically possessed high specific surface area, adequate electrical conductivity and hydrophobic properties. The addition of D-(+)-Glucose anhydrous in hydrothermal process can attach carbon to the surface of the WO_3/Bi_2WO_6 to form a stable hydrophobic layer, blocking the adsorption and penetration of water molecules during the sensing process. The improved electrical conductivity after C cladding can enhance the signal transmission efficiency and response speed, which can maintain the performance of the sensor in high humidity environment.

4. Conclusions

In summary, we incorporated C cladding on the bismuth tungstate-based 3D twisted micro-flowers. The carbon-based material along with heterojunction ($C_{0.75}/WO_3/Bi_2WO_6$) collectively enhanced the benzaldehyde sensing performance with high sensitivity (33.7 @ 50 ppm), superior exclusive detection, fast recovery time of 49 s, excellent stability exceeding 15 days (average response level of 83.5 @ 75 ppm) and anti-humidity features (CVs of 3.8) substantially. Induced UV light further increased the high mobility and low initial carrier concentration and decreased the operating temperature of the proposed system simultaneously. The fundamental VOC sensing mechanism was elaborated through experimental proof, simulation analysis and logical demonstration in part 3.3. The potential of as-prepared sensor for practical application was verified by agricultural product quality inspection. Overall, this work disclosed the deep insights and a unique approach that benefited VOCs sensing and stabilization conducting by functionalization of C cladding, which not only altered the conventional definition toward the sensing mechanism but also offered a groundbreaking concept for the creation of high-performance resistive-type sensor.

CRediT authorship contribution statement

Zichen Zheng: Writing – original draft, Visualization, Methodology, Investigation, Data curation, Conceptualization. **Kewei Liu:** Writing – review & editing, Formal analysis, Data curation. **Chao Zhang:** Writing – review & editing, Validation, Supervision, Methodology, Investigation, Funding acquisition. **Marc Debliquy:** Writing – review & editing, Visualization, Validation, Supervision.

Declaration of Competing Interest

The authors declare that they have no known competing financial interests or personal relationships that could have appeared to influence the work reported in this paper.

Data availability

Data will be made available on request.

Acknowledgments

This work was supported by the Outstanding Youth Foundation of Jiangsu Province of China (No. BK20211548), the Yangzhou Science and Technology Plan Project (No. YZ2023246), the China Scholarship Council (No. 202308320445) and Postgraduate Research and Practice Innovation Program of Jiangsu Province of China (No. KYCX23_3551).

Appendix A. Supporting information

Supplementary data associated with this article can be found in the online version at doi:10.1016/j.snb.2024.135982.

References

[1] A. Andersen, Final report on the safety assessment of benzaldehyde, Int. J. Toxicol. 25 (2006) 11–27, https://doi.org/10.1080/10915810600716612.
[2] Y. Li, X. Liu, Q. Wu, J. Yi, G. Zhang, Discrimination and detection of benzaldehyde derivatives using sensor array based on fluorescent carbon nanodots, Sens. Actuators, B 261 (2018) 271–278, https://doi.org/10.1016/j.snb.2018.01.160.
[3] C. Wang, J. Sun, Y. Sun, Z. Tan, X. Xu, Y. Fu, Z. Feng, J. Zhu, Fabrication of cubic Co_3O_4-hexagonal ZnO disk/rGO as a two-phase benzaldehyde sensor via a sequential nucleation strategy, Sens. Actuators, B 330 (2021) 129384, https://doi.org/10.1016/j.snb.2020.129384.

[4] Y. Wu, S. Zhang, X. Wang, N. Na, Z. Zhang, Development of a benzaldehyde sensor utilizing chemiluminescence on nanosized Y_2O_3, Luminescence 23 (2008) 376–380, https://doi.org/10.1002/bio.1047.

[5] P.Y. Du, W. Gu, X. Liu, Highly selective luminescence sensing of nitrite and benzaldehyde based on 3d-4f heterometallic metal-organic frameworks, Dalton Trans. 45 (2016) 8700–8704, https://doi.org/10.1039/c6dt01360k.

[6] C. Fang, S. Wang, Q. Wang, J. Liu, B. Geng, Coralloid SnO_2 with hierarchical structure and their application as recoverable gas sensors for the detection of benzaldehyde/acetone, Mater. Chem. Phys. 122 (2010) 30–34, https://doi.org/10.1016/j.matchemphys.2010.03.005.

[7] F. Yang, Z. Guo, Engineering NiO sensitive materials and its ultra-selective detection of benzaldehyde, J. Colloid Interface Sci. 467 (2016) 192–202, https://doi.org/10.1016/j.jcis.2016.01.033.

[8] K.V. Gobi, K. Matsumoto, K. Toko, H. Ikezaki, N. Miura, Enhanced sensitivity of self-assembled-monolayer-based SPR immunosensor for detection of benzaldehyde using a single-step multi-sandwich immunoassay, Anal. Bioanal. Chem. 387 (2007) 2727–2735, https://doi.org/10.1007/s00216-007-1159-5.

[9] Y.K. Jo, S.-Y. Jeong, Y.K. Moon, Y.-M. Jo, J.-W. Yoon, J.-H. Lee, Exclusive and ultrasensitive detection of formaldehyde at room temperature using a flexible and monolithic chemiresistive sensor, Nat. Commun. 12 (2021) 4955, https://doi.org/10.1038/s41467-021-25290-3.

[10] H. Zhang, Z. Zhang, Z. Li, H. Han, W. Song, J. Yi, A chemiresistive-potentiometric multivariate sensor for discriminative gas detection, Nat. Commun. 14 (2023) 3495, https://doi.org/10.1038/s41467-023-39213-x.

[11] K. Liu, Z. Zheng, M. Debliquy, C. Zhang, Highly-sensitive volatile organic compounds evaluation by three-dimensional $ZnFe_2O_4/ZnSnO_3$ heterostructures and their predictive grain quality monitoring, Chem. Eng. J. 453 (2023) 139824, https://doi.org/10.1016/j.cej.2022.139824.

[12] K. Großmann, S. Wicker, U. Weimar, N. Barsan, Impact of Pt additives on the surface reactions between SnO_2, water vapour, CO and H_2; an operando investigation, Phys. Chem. Chem. Phys. 15 (2013) 19151–19158, https://doi.org/10.1039/C3CP52782D.

[13] D. Zhang, J. Tong, B. Xia, Humidity-sensing properties of chemically reduced graphene oxide/polymer nanocomposite film sensor based on layer-by-layer nano self-assembly, Sens. Actuators, B 197 (2014) 66–72, https://doi.org/10.1016/j.snb.2014.02.078.

[14] H. Bi, K. Yin, X. Xie, J. Ji, S. Wan, L. Sun, M. Terrones, M.S. Dresselhaus, Ultrahigh humidity sensitivity of graphene oxide, Sci. Rep. 3 (2013) 2714, https://doi.org/10.1038/srep02714.

[15] Y. Wang, Y. Zhou, G. Xie, J. Li, Y. Wang, X. Liu, Z. Zang, Dual resistance and impedance investigation: ultrasensitive and stable humidity detection of molybdenum disulfide nanosheet-polyethylene oxide hybrids, ACS Appl. Mater. Interfaces 13 (2021) 25250–25259, https://doi.org/10.1021/acsami.1c02119.

[16] Y. Zhou, Y. Wang, Y. Wang, H. Yu, R. Zhang, J. Li, Z. Zang, X. Li, MXene $Ti_3C_2T_x$-derived nitrogen-functionalized heterophase TiO_2 homojunctions for room-temperature trace ammonia gas sensing, ACS Appl. Mater. Interfaces 13 (2021) 56485–56497, https://doi.org/10.1021/acsami.1c17429.

[17] Y. Byoun, S.-W. Choi, Y. Tae Byun, Realisation of highly sensitive and selective NO_2 detection at room temperature utilizing defect-induced single-walled carbon nanotubes combined with Pt functionalisation, Appl. Surf. Sci. 590 (2022) 153068, https://doi.org/10.1016/j.apsusc.2022.153068.

[18] N. Liu, Y. Li, Y. Li, L. Cao, N. Nan, C. Li, L. Yu, Tunable NH_4F-assisted synthesis of 3D porous In_2O_3 microcubes for outstanding NO_2 gas-sensing performance: fast equilibrium at high temperature and resistant to humidity at room temperature, ACS Appl. Mater. Interfaces 13 (2021) 14355–14364, https://doi.org/10.1021/acsami.0c22987.

[19] Z. Wang, C. Xie, B. Liu, Y. Jiang, Z. Li, H. Tai, X. Li, Self-adaptive temperature and humidity compensation based on improved deep BP neural network for NO_2 detection in complex environment, Sens. Actuators, B 362 (2022) 131812, https://doi.org/10.1016/j.snb.2022.131812.

[20] X. Chen, J. Hu, P. Chen, M. Yin, F. Meng, Y. Zhang, UV-light-assisted NO_2 gas sensor based on WS_2/PbS heterostructures with full recoverability and reliable anti-humidity ability, Sens. Actuators, B 339 (2021) 129902, https://doi.org/10.1016/j.snb.2021.129902.

[21] J.-S. Kim, K.B. Kim, H.-Y. Li, C.W. Na, K. Lim, Y.K. Moon, J.W. Yoon, J.-H. Lee, Pure and Pr-doped $Ce_4W_9O_{33}$ with superior hydroxyl scavenging ability: humidity-independent oxide chemiresistors, J. Mater. Chem., A 9 (2021) 16359–16369, https://doi.org/10.1039/D1TA02618F.

[22] Y. Sun, Z. Zhao, K. Suematsu, P. Li, Z. Yu, W. Zhang, J. Hu, K. Shimanoe, Rapid and stable detection of carbon monoxide in changing humidity atmospheres using clustered In_2O_3/CuO nanospheres, ACS Sens 5 (2020) 1040–1049, https://doi.org/10.1021/acssensors.9b02557.

[23] J. Wu, Z. Wu, H. Ding, Y. Wei, W. Huang, X. Yang, Z. Li, L. Qiu, X. Wang, Three-dimensional graphene hydrogel decorated with SnO_2 for high-performance NO_2 sensing with enhanced immunity to humidity, ACS Appl. Mater. Interfaces 12 (2020) 2634–2643, https://doi.org/10.1021/acsami.9b18098.

[24] W. Liu, L. Xu, K. Sheng, C. Chen, X. Zhou, B. Dong, X. Bai, S. Zhang, G. Lu, H. Song, APTES-functionalized thin-walled porous WO_3 nanotubes for highly selective sensing of NO_2 in a polluted environment, J. Mater. Chem., A 6 (2018) 10976–10989, https://doi.org/10.1039/C8TA02452A.

[25] H. Zhou, Z. Wen, J. Liu, J. Ke, X. Duan, S. Wang, Z-scheme plasmonic Ag decorated WO_3/Bi_2WO_6 hybrids for enhanced photocatalytic abatement of chlorinated-VOCs under solar light irradiation, Appl. Catal., B-Environ. 242 (2019) 76–84, https://doi.org/10.1016/j.apcatb.2018.09.090.

[26] W. Guo, L. Jian, X. Wang, W. Zeng, Hydrothermal synthesis of Ni-doped hydrangea-like Bi_2WO_6 and the enhanced gas sensing property to n-butanol, Sens. Actuators, B 357 (2022) 131396, https://doi.org/10.1016/j.snb.2022.131396.

[27] A. Marikutsa, L. Yang, A.N. Kuznetsov, M. Rumyantseva, A. Gaskov, Effect of W−O bonding on gas sensitivity of nanocrystalline Bi_2WO_6 and WO_3, J. Alloy. Compd. 856 (2021) 158159, https://doi.org/10.1016/j.jallcom.2020.158159.

[28] Y. Li, X. Wang, G. Sun, J. Cao, Y. Wang, In situ modification of discoid α-Fe_2O_3 nanostructures with Bi_2WO_6 for high performance n-butanol sensor, Vacuum 216 (2023) 112478, https://doi.org/10.1016/j.vacuum.2023.112478.

[29] X. Qian, D. Yue, Z. Tian, M. Reng, Y. Zhu, M. Kan, T. Zhang, Y. Zhao, Carbon quantum dots decorated Bi_2WO_6 nanocomposite with enhanced photocatalytic oxidation activity for VOCs, Appl. Catal., B-Environ. 193 (2016) 16–21, https://doi.org/10.1016/j.apcatb.2016.04.009.

[30] P. Jineesh, T.C. Bhagya, R. Remya, S.M.A. Shibli, Photocatalytic hydrogen generation by WO_3 in synergism with hematite-anatase heterojunction, Int. J. Hydrog. Energ. 45 (2020) 18946–18960, https://doi.org/10.1016/j.ijhydene.2020.05.043.

[31] T.H. Eom, S.H. Cho, J.M. Suh, T. Kim, J.W. Yang, T.H. Lee, S.E. Jun, S.J. Kim, J. Lee, S.-H. Hong, H.W. Jang, Visible light driven ultrasensitive and selective NO_2 detection in tin oxide nanoparticles with sulfur doping assisted by l-cysteine, Small 18 (2022) 2106613, https://doi.org/10.1002/smll.202106613.

[32] M.-S. Gui, W.-D. Zhang, Y.-Q. Chang, Y.-X. Yu, One-step hydrothermal preparation strategy for nanostructured WO_3/Bi_2WO_6 heterojunction with high visible light photocatalytic activity, Chem. Eng. J. 197 (2012) 283–288, https://doi.org/10.1016/j.cej.2012.05.032.

[33] X. Wang, J. Lu, W. Han, P. Cheng, Y. Wang, J. Sun, J. Ma, P. Sun, H. Zhang, Y. Sun, G. Lu, Carbon modification endows WO_3 with anti-humidity property and long-term stability for ultrafast H_2S detection, Sens. Actuators, B 350 (2022) 130884, https://doi.org/10.1016/j.snb.2021.130884.

[34] G. Liu, E. Froudarakis, J.M. Patel, M.Y. Kochukov, B. Pekarek, P.J. Hunt, M. Patel, K. Ung, C.-H. Fu, J. Jo, H.-K. Lee, A.S. Tolias, B.R. Arenkiel, Target specific functions of EPL interneurons in olfactory circuits, Nat. Commun. 10 (2019) 3369, https://doi.org/10.1038/s41467-019-11354-y.

[35] Z. Zheng, K. Liu, Y. Zhou, M. Debliquy, C. Zhang, Ultrasensitive room-temperature geranyl acetone detection based on Fe@WO_{3-x} nanoparticles in cooked rice flavor analysis, J. Adv. Ceram. 12 (2023) 1547–1561, https://doi.org/10.26599/jac.2023.9220771.

[36] X. Chen, J. Li, F. Chen, Photocatalytic degradation of MB by novel and environmental ZnO/Bi_2WO_6-CC hierarchical heterostructures, Mater. Charact. 189 (2022) 111961, https://doi.org/10.1016/j.matchar.2022.111961.

[37] G. Zhang, F. Lü, M. Li, J. Yang, X. Zhang, B. Huang, Synthesis of nanometer Bi_2WO_6 synthesized by sol–gel method and its visible-light photocatalytic activity for degradation of 4BS, J. Phys. Chem. Solids 71 (2010) 579–582, https://doi.org/10.1016/j.jpcs.2009.12.041.

[38] J. Yan, M.-T.F. Rodrigues, Z. Song, H. Li, H. Xu, H. Liu, J. Wu, Y. Xu, Y. Song, Y. Liu, P. Yu, W. Yang, R. Vajtai, H. Li, S. Yuan, P.M. Ajayan, Reversible formation of g-C_3N_4 3D hydrogels through ionic liquid activation: gelation behavior and room-temperature gas-sensing properties, Adv. Funct. Mater. 27 (2017) 1700653, https://doi.org/10.1002/adfm.201700653.

[39] P.-F. Cao, S.-Y. Ma, R.-J. Fan, Carbon-doped porous hollow alpha-Fe_2O_3 microtubules controlled by absorbent cotton bio-template to detect acetic acid vapor, Ceram. Int. 48 (2022) 12729–12741, https://doi.org/10.1016/j.ceramint.2022.01.142.

[40] S. Laurenzi, S. Botti, A. Rufoloni, M.G. Santonicola, Mapping the residual strain of carbon nanotubes in DWCNT/epoxy nanocomposites after tensile load using Raman microscopy, Compos. Commun. 21 (2020) 100424, https://doi.org/10.1016/j.coco.2020.100424.

[41] J. Huang, Y. Xiao, Z. Peng, Y. Xu, L. Li, L. Tan, K. Yuan, Y. Chen, Co_3O_4 supraparticle-based bubble nanofiber and bubble nanosheet with remarkable electrochemical performance, Adv. Sci. 6 (2019) 1900107, https://doi.org/10.1002/advs.201900107.

[42] D.-H. Kim, S. Chong, C. Park, J. Ahn, J.-S. Jang, J. Kim, I.-D. Kim, Oxide/ZIF-8 hybrid nanofiber yarns: heightened surface activity for exceptional chemiresistive sensing, Adv. Mater. 34 (2022) 2105869, https://doi.org/10.1002/adma.202105869.

[43] H. Pazniak, A.S. Varezhnikov, D.A. Kolosov, I.A. Plugin, A.D. Vito, O.E. Glukhova, P.M. Sheverdyaeva, M. Spasova, I. Kaikov, E.A. Kolesnikov, P. Moras, A. M. Bainyashev, M.A. Solomatin, I. Kiselev, U. Wiedwald, V.V. Sysoev, 2D molybdenum carbide MXenes for enhanced selective detection of humidity in air, Adv. Mater. 33 (2021) 2104878, https://doi.org/10.1002/adma.202104878.

[44] X. Wang, P. Ren, H. Tian, H. Fan, C. Cai, W. Liu, Enhanced gas sensing properties of SnO_2: the role of the oxygen defects induced by quenching, J. Alloy. Compd. 669 (2016) 29–37, https://doi.org/10.1016/j.jallcom.2016.01.225.

[45] C. Zhang, K. Liu, Z. Zheng, M. Debliquy, Defect engineering of nanostructured $ZnSnO_3$ for conductometric room temperature CO_2 sensors, Sens. Actuators, B 384 (2023) 133628, https://doi.org/10.1016/j.snb.2023.133628.

[46] Y. Qian, Y. Han, X. Zhang, G. Yang, G. Zhang, H.L. Jiang, Computation-based regulation of excitonic effects in donor-acceptor covalent organic frameworks for enhanced photocatalysis, Nat. Commun. 14 (2023) 3083, https://doi.org/10.1038/s41467-023-38884-w.

[47] H. Zhao, J. Sun, J. Liu, H. Zhang, H. He, X. Liu, D. Liao, Z. Tong, L. Sun, UV-triggered carrier transport regulation of fibrous NiO/SnO_2 heterostructures for triethylamine detection, Chem. Eng. J. 476 (2023) 146687, https://doi.org/10.1016/j.cej.2023.146687.

[48] A. Šetkus, Heterogeneous reaction rate based description of the response kinetics in metal oxide gas sensors, Sens. Actuators B 87 (2002) 346–357, https://doi.org/10.1016/S0925-4005(02)00269-1.
[49] S. Shao, C. Xie, L. Zhang, S. Wei, H.W. Kim, S.S. Kim, $CsPbI_3$NC-sensitized SnO_2/multiple-walled carbon nanotube self-assembled nanomaterials with highly selective and sensitive NH_3 sensing performance at room temperature, ACS Appl. Mater. Interfaces 13 (2021) 14447–14457, https://doi.org/10.1021/acsami.0c20566.
[50] M.-S. Yao, W.-X. Tang, G.-E. Wang, B. Nath, G. Xu, MOF thin film-coated metal oxide nanowire array: significantly improved chemiresistor sensor performance, Adv. Mater. 28 (2016) 5229–5234, https://doi.org/10.1002/adma.201506457.
[51] C. Zhang, Z. Zheng, K. Liu, M. Debliquy, Q. Liu, Highly sensitive and selective Sb_2WO_6 microspheres in detecting VOC biomarkers in cooked rice: experimental and density functional theory study, Food Chem. 424 (2023) 136323, https://doi.org/10.1016/j.foodchem.2023.136323.
[52] X.-X. He, H.-F. Chai, Y.-W. Zhou, K.-W. Liu, Z.-X. Yu, C. Zhang, Sensing properties and mechanisms of LaF_3–Co_3O_4 nanorods for low-concentration methanol detection, Rare Met. 43 (2024) 2193–2204, https://doi.org/10.1007/s12598-023-02593-6.
[53] K. Xu, M. Han, Z. Zheng, Z. Yu, H. Liao, H. Sun, C. Zhang, Well-designed g-C_3N_4 nanosheet incorporated Ag loaded $Er_{0.05}La_{0.95}FeO_3$ heterojunctions for isoamyl alcohol detection, J. Adv. Ceram. (2024), https://doi.org/10.26599/JAC.2024.9220892.
[54] X. Li, B. Kang, F. Dong, Z. Zhang, X. Luo, L. Han, J. Huang, Z. Feng, Z. Chen, J. Xu, B. Peng, Z.L. Wang, Enhanced photocatalytic degradation and H_2/H_2O_2 production performance of S-pCN/$WO_{2.72}$ S-scheme heterojunction with appropriate surface oxygen vacancies, Nano Energy 81 (2021) 105671, https://doi.org/10.1016/j.nanoen.2020.105671.
[55] Y. Zhou, Y. Luo, Z. Zheng, K. Liu, X. He, K. Wu, M. Debliquy, C. Zhang, Urchin-like Na-doped zinc oxide nanoneedles for low-concentration and exclusive VOC detections, J. Adv. Ceram. 13 (2024) 507–517, https://doi.org/10.26599/JAC.2024.9220873.
[56] J.-Y. Xu, K.-C. Xu, X.-X. He, H.-L. Liao, M. Debliquy, Q.-Q. Liu, C. Zhang, Interface engineering of ZnSnO3-based heterojunctions for room-temperature methanol monitoring, Rare Met. 42 (2023) 4153–4166, https://doi.org/10.1007/s12598-023-02344-7.

Zichen Zheng received his B.S. degree in 2020 at Hefei University of Technology (China). He is currently pursuing his Ph.D degree at Yangzhou University (China) and University of Mons (Belgium). He takes interests in smart materials for high-performance gas sensors working at room temperature applying for food quality and plant pest detection.

Kewei Liu received her B.S. degree in 2019 at Yangzhou University (China). She is currently pursuing her Ph.D degree at Yangzhou University (China) and University of Mons (Belgium). She takes interests in MOS-based materials for high-performance gas sensors and array for unhusked rice mildew detection.

Marc Debliquy received his Ph.D. degree at Faculty of Engineering in Mons (Belgium) in1999 in the field of organic semiconductors for fire detection. He joined the Sochinor Company in 2000. He left in 2003 for joining Materia Nova. He was responsible for the research activities in the field of gas sensors. Since October 2008, he joined the Material Science Department of Faculty of Engineering of University of Mons and worked as a team leader of semiconductor and sensor group. He was promoted as an associate professor in September 2013. His main research interest is smart coatings for chemical detection. He is also co-founder of the spin-off company B-Sens specialized in optical fiber sensors.

Chao Zhang received a B.S. degree from the Chongqing University (China) in 2003 and a joint Ph.D. degree from Technology University of Belfort-Montbéliard (France) and Xi'an Jiaotong University (China) in June 2008. From September 2007 to January 2009, he worked as a teaching-research assistant in Technology University of Belfort-Montbéliard. Since Feb 2009, he is postdoctoral researcher, and then a senior researcher in Materials Science Department of engineering School of University of Mons (Belgium). In 2014, he joined Yangzhou University China) as professor where he is leading a research group on thermal spray coatings and gas sensors. He is Vice Dean (August 2016 to September 2022) and Dean (September 2022 to present) of College of Mechanical Engineering. His research interests include thermal-sprayed techniques and coatings, especially gas sensing and wear-resistant coatings.